Self-Assembly of a Barnacle Cement Protein (MrCP20) into Adhesive Nanofibrils with Concomitant Regulation of CaCO 3 Polymorphism

Harini Mohanram, Tristan Georges, Konstantin Pervushin, Thierry Azaïs, Ali Miserez

Self-Assembly of a Barnacle Cement Protein (MrCP20) into Adhesive Nanofibrils with Concomitant Regulation of $CaCO_3$ Polymorphism

Harini Mohanram[1], Tristan Georges[2], Konstantin Pervushin[1], Thierry Azaïs[2], Ali Miserez*[1,3]

[1]School of Biological Sciences, Nanyang Technological University (NTU), 59 Nanyang Drive, Singapore 636921.

[2] Sorbonne Université, CNRS, Collège de France, Laboratoire de Chimie de la Matière Condensée de Paris (LCMCP), 4 place Jussieu, F-75005, Paris, France.

[3]Center for Sustainable Materials (SusMat), School of Materials Science and Engineering, Nanyang Technological University (NTU), 50 Nanyang Avenue, Singapore 637553.

*Corresponding author: ali.miserez@ntu.edu.sg

Keywords: *M.rosa* cement protein (MrCP) | $CaCO_3$ Mineralization - Non classical pathway | Transient liquid phase | NMR spectroscopy | Protovaterite-ACC| Self-assembly | Nanofibrils.

Abstract

Barnacles are convenient model organisms to study both biomineralization and bioadhesion phenomena. They secrete a proteinaceous adhesive from cement proteins (CPs) to strongly attach to solid immersed substrates. More recently, it has been suggested that some CPs also play a key role in regulating calcification of barnacles' protective shells. In this study, combining both solution and solid-state NMR, Raman and infrared spectroscopy studies, and AFM and TEM imaging, we have explored $CaCO_3$ mineralization pathway regulated by *Megabalanus rosa* cement protein 20 (MrCP20). Our data show that MrCP20 can sequestrate inorganic calcium and carbonate ions from the solution state, which quickly coarsen into liquid-like microdroplets and subsequently form protovaterite amorphous $CaCO_3$ (ACC) particles. This pathway leads to the stabilization of the metastable vaterite polymorphism of $CaCO_3$. Simultaneously, AFM and TEM investigations show that MrCP20 undergoes fibrillization triggered by pH drift arising during $CaCO_3$ mineralization, leading to amyloid-like nanofibrils. Based on protein NMR, this mechanism appears to be stabilized by the reduction of intra-molecular disulfide bonds. Collectively, our results demonstrate that MrCP20 plays a synergistic role of regulating $CaCO_3$ biomineralization while concomitantly self-assembling into adhesive nanofibrils.

Introduction

During biomineralization, the deposition of mineral nanocrystals into multi-scale hard tissues, such as seashells or bones of vertebrates, is finely regulated by a proteinaceous organic matrix[1-2]. Nacreous and prismatic shells are well-established model systems to study biomineralization processes owing to their outstanding mechanical properties, accessibility, and suitability to monitor spatial-temporal mineral deposition in laboratory setups[3-6]. The majority of these exoskeletons are built from calcium carbonate ($CaCO_3$) crystals of different polymorphism, namely calcite (the thermodynamically stable phase) or aragonite and vaterite (the metastable phases)[7]. The formation of biogenic $CaCO_3$ crystals can follow two pathways: *(i)* classical nucleation theory (CNT) whereby ions aggregate to form a crystal nucleus, which upon reaching supersaturation becomes a mature crystal[8-9], or *(ii)* non-classical pathways[10] where pre-nucleation clusters (PNCs) of Ca^{2+} and CO_3^{2-} ions precede the nucleation of amorphous calcium carbonate (ACC) nuclei from a liquid precursor that subsequently grow into mature crystals[11-14]. In particular, the presence of organic additives such as poly-aspartic acid, poly-acrylic acid, or intrinsically disordered proteins (IDPs) tends to favor a polymer induced liquid precursor (PILP) mechanism, whereby ACC formation is induced via a liquid-liquid phase separation (LLPS) process along a non-classical pathway[15-19].

Barnacles are holdfast macrofoulers with a protective hard shell fastened to foreign substrata for their survival. Barnacles grow through distinct phases. During metamorphosis, the exploring cyprids secrete temporary proteinaceous footprints that contain settlement inducing proteins (SIPCs) which later mediate biomineralization of a skeletal network in adult acorn barnacles[20-21]. The hard

exoskeleton of matured barnacle enclosing the soft prosoma (main body) is made up of calcite shells that radiate from the base plate[22-27].

The sticky nature of barnacles is established through secretion of a multi-protein cement-like complex from their base plates[28-31], which allows barnacles to attach themselves to a wide range of solid immersed substrates. Unlike other marine fouling species, post-translational modifications have thus far not been identified in barnacle cement proteins (CPs)[32-33]. The base plate of *Megabalanus rosa* (*M. rosa*), a well-studied acorn barnacle, secretes at least five proteins of varying molecular weight (MW) in the cement called MrCPs[34]. Based on their amino acid compositions, it was suggested that MrCP19 and MrCP20 are low MW proteins that are located at the interfaces with the substratum and the animal, respectively[30]. Since nanofibrils have been observed on the surface of the cement, it has also been suggested that cement proteins self-assemble into amyloid-like nanofibrils that mediate interfacial adhesion[35-36]. The primary structure of MrCP20 is dominated by a high content of 32 cysteine (Cys) residues as well as a high molar concentration of acidic side-chains, prompting Kamino *et al*.[28-30, 34] to propose that MrCP20 may function as an adhesive layer to positively-charged solid substrates. Our group recently reported the 3D solution structure of the recombinant version of MrCP20 (*r*MrCP20) by solution-state Nuclear Magnetic Resonance (NMR) spectroscopy and found it to be folded into three structural domains intervened by two dynamic linker regions[37]. The structural domains are dominated by anti-parallel β-strands stabilized by intramolecular disulfide bonds, with the β-strands enriched with acidic amino acids that impart a negative surface potential to *r*MrCP20. Further, molecular dynamic (MD) simulation

studies predicted that *r*MrCP20 adopts multiple dynamic conformations, hinting at its heterologous function[37].

Adsorption isotherm studies by Mori *et al.*[38] identified MrCP20 selectivity towards calcite over other positively-charged surfaces, whereas in a detailed Atomic Force Microscopy (AFM) study, So *et al*. revealed that MrCP20 interacts with the $\{\overline{1014}\}$ face of calcite and observed a structural transition of the protein into nanofibrils[39]. In addition, our recent MD studies of MrCP20 with calcium and carbonate ions predicted ion sequestration activity by the charged residues of the protein[40], with the majority of ion clustering occurring around the turn regions of MrCP20. Furthermore, MrCP20 was predicted to strongly bind to calcite through synergistic attractive interactions, including: *(i)* Coulombic attraction of anionic residues to the calcite surface, *(ii)* cationic side chains of lysine (Lys) interacting with CO_3^{2-} ions, and *36* water-mediated hydrogen bonding of the polar side chains serine (Ser), threonine (Thr), and tyrosine (Tyr)[40]. Because of these characteristics, MrCP20 has been postulated not only to play an important role in adhering to solid oxide surfaces, but also to regulate mineralization of the barnacle shell.

In the present study, we aimed to experimentally establish whether MrCP20 regulates $CaCO_3$ crystal formation as predicted by MD simulations. Combining ^{13}C solution and solid-state NMR, Raman, and Attenuated Total Reflection Infrared (ATR-FTIR) spectroscopy studies with transmission electron microscopy (TEM), we find that *r*MrCP20 (recombinant MrCP20) stabilizes the metastable vaterite polymorph of $CaCO_3$. In addition to stabilizing metastable vaterite, we also establish by AFM and TEM imaging that *r*MrCP20 concomitantly exhibits a structural transition towards nanofibrils. By monitoring structural transitions of *r*MrCP20 upon incubation

with carbonate ions by solution NMR, we finally identify the reduction of di-sulfide bonds, as well their flanking acidic domains, as playing a critical role in both $CaCO_3$ crystal growth and fibrillization of *r*MrCP20. Overall, our studies on *r*MrCP20-mediated vaterite mineralization provides molecular-level insights into the formation of metastable functional biogenic minerals.

Methods

rMrCP20 expression and purification

The detailed expression and purification protocol of *r*MrCP20 was described in Mohanram *et al*.[37]. Briefly, single colony transformants of *r*MrCP20 were expressed overnight in Luria-Bertani [10] medium with 100 μg/mL ampicillin and 1 mM IPTG (Isopropyl thio-β-D-galactoside) at 20°C. The cells were then sonicated and the crude lysate after high-speed centrifugation was purified by affinity chromatography (Ni-NTA affinity column). The eluted protein was further purified to homogeneity using size-exclusion chromatography (SEC) (Superdex 75, 16/600) using isocratic elution in 20 mM Tris, 150 mM NaCl, at pH 8.3. The purified protein was then buffer exchanged with 0.1 M $CaCl_2$ and concentrated using Vivaspin column (MW cutoff 5 kDa).

Calcium carbonate mineralization experiments

In vitro mineralization experiments were carried out by preparing aliquots of equal volumes of 0.1 M $CaCl_2$ (pH 8.3) and 0.1 M $NaHCO_3$ (pH 9.2) either in the presence or absence of 4 mg/mL of *r*MrCP20. The solutions were left undisturbed for appropriate period of times (4 h, 1 day, 4 days and 7 days). For solid state NMR experiments, isotope labeled $NaH^{13}CO_3$ was used. After desired period of

incubations, $CaCO_3$ crystals were collected by centrifugation at 7K rpm for 5 mins followed by several rounds of washing and resuspending with water.

Dynamic light scattering (DLS)

The hydrodynamic diameter (D_H) of the particles formed during $CaCO_3$ mineralization in the presence and absence of *r*MrCP20 was measured by DLS on a Brookhaven 90 plus (NY, USA) instrument. 50 μL of 0.1 M $CaCl_2$ (with and without 4 mg/mL *r*MrCP20) was mixed with 50 μL of 0.1 M $NaHCO_3$ and measured every 5 mins until 1 h and every 30 mins thereafter until 6 h. The sample was mixed gently before each measurement.

Isothermal titration calorimetry (ITC)

Thermodynamics of $CaCO_3$ formation in the presence of *r*MrCP20 was analyzed using ITC experiments on Nano ITC (TA Instruments, Lindon, USA). The sample cell was filled with 200 μL of 0.05 mM $NaHCO_3$ and reference cell was filled with water. The injectant was filled with 50 μL of 4 mg/mL of *r*MrCP20 suspended in 0.25 M $CaCl_2$. Typically, 30 injections of 1.5 μL was carried out with equilibration time of 300 s. *Nanoanalyze* software was used to integrate the raw data and fit the models.

Spectroscopy Methods

Attenuated total reflection – Fourier transform infrared (ATR-FTIR) spectroscopy

Initial morphogenesis of $CaCO_3$ formation for samples in the presence and absence of *r*MrCP20 was followed by acquisition of ATR-FTIR spectra on a Bruker Vertex 70 (Massachusetts, USA) equipped with a MIRacle^{TM} 3-reflection ZnSe-

Diamond accessory coupled to liquid N_2 cooled mercury cadmium telluride (MCT) detector. The optical bench was purged with nitrogen gas throughout the experiment. Simple scan measurements were obtained over the range of 4000 to 400 cm^{-1} with a resolution of 4 cm^{-1}, averaged over 256 scans. Samples were aliquoted from 4 h, 6 h,1 day, 4 days and 7 days of incubation. *OPUS 6.5* software was used to process all the spectra for water vapor subtraction and baseline correction. Spectra from samples of 6 h and 1 day were deconvoluted in amide I region (1700-1600 cm^{-1}) by secondary derivation and peak fitting was performed with 100% gaussian curves.

Raman spectroscopy

Raman spectra for samples in the presence and absence of *r*MrCP20 were obtained using a confocal Raman microscope (alpha300, WITec) equipped with a 488 nm laser source and a 100X objective lens. Around 10 μL of samples from 4 h, 1 day, 4 days and 7 days of $CaCO_3$ crystals of both protein and control samples were deposited on to glass slides and dried. The spots were imaged using 100X objective microscope and spectra were acquired with an integration time of 1 s and 106 accumulations. The spectrometer was calibrated using a silicon wafer sample using its 0 cm^{-1} (the Rayleigh scattering) and 520 cm^{-1} (Si-Si vibrational band) peaks. The *WITec Project 2.10* was used for filtering, analysis and plotting the data.

Solid state Nuclear Magnetic Resonance (NMR) spectroscopy

All of the solid state ^{13}C NMR spectra were acquired at room temperature on Bruker Avance-III 300 spectrometer operating at ^{13}C Larmor frequency of 75 MHz. ^{13}C enriched $CaCO_3$ crystals in the presence or absence of *r*MrCP20 obtained at 4 h, 1 day, 4 days and 7 days were packed into 4.0 mm zirconia rotors closed with a kel-f

cap and spun at the magic angle (MAS). Due to the small amount of material, kel-f inserts were used to fix the sample at the center of the rotor. 30°-direct excitation (DE) MAS spectra were recorded with high power proton decoupling (75 kHz; spinal-64) and were acquired with relaxation delay of 200 s to ensure a full relaxation along the *z* axis, 50 ms of FID acquisition time and 800 transient accumulations at a magic angle spinning frequency of 12.5 kHz. ^{1}H -^{13}C cross polarization (CP) MAS NMR spectra were recorded with relaxation delay of 10 s, 50 ms acquisition time, 3 ms of contact time and 7744 transient accumulations at a magic-angle spinning frequency of 5 kHz. All of the ^{13}C NMR spectra were referenced to TMS.

Solution state NMR spectroscopy

A series of 1D ^{13}C NMR spectra were acquired on Bruker 400 MHz spectrometer. ^{13}C enriched $NaHCO_3$ was used for sample preparation. Spectra were acquired every 5 mins for both samples in the presence and absence of *r*MrCP20. 2D ^{1}H-^{15}N HSQC spectra of *r*MrCP20 in 0.1 M $CaCl_2$ in the presence and absence of 0.1 M $NaHCO_3$ were recorded on Bruker 700 MHz spectrometer. There were 512 increments in F1 and 2048 in F2 axes with the number of scans set to 32. All of the spectra were referenced to DSS.

Microscopy Methods

Scanning Electron Microscopy (SEM)

The morphology of calcium carbonate crystals obtained at 4 h, 1 day, 4 days and 7 days of samples in the presence and absence of *r*MrCP20 were characterized using a field emission SEM (FESEM, JEOL 6400F) at an accelerating voltage of 5 kV. About 50 μL of samples were dried on the coverslips overnight which were then

secured onto the SEM mounts using carbon and copper tapes ensuring a conductive pathway for imaging. The mounts were coated with platinum below 5 Pa, at 20 mA for 35 s and imaged in SEI mode at working distance of 8 mm.

Atomic force microscopy (AFM)

The morphological changes leading to the formation of $CaCO_3$ crystals upon addition of 4 mg/mL *r*MrCP20 in 0.1 M $CaCl_2$ to 0.1 M $NaHCO_3$ was followed hourly (1 h, 2 h, 4 h, 6 h and 24 h) using Park NX10 AFM system (Suwon, Korea). All images were acquired in tapping mode with Pointprobe NCSTR Si3N4 cantilevers (RF – 160 kHz, Force constant – 7.4 N/m). 10 μL of samples at appropriate times were deposited on freshly cleaved mica surface and air dried overnight. The images were processed using Park XEI software.

Amyloid fibrils of *r*MrCP20 during $CaCO_3$ mineralization was also imaged using AFM. The protein samples from 6 h and 24 h were diluted 50 times with DI water and deposited onto freshly cleaved mica surface and imaged after drying it overnight.

Transmission electron microscopy (TEM)

About 4 mg/mL of *r*MrCP20 in 0.1 M $CaCl_2$ and 0.1 M $NaHCO_3$ was incubated for 24 hours. It was then diluted 50 times and aliquot of 3 μL was deposited onto TEM copper grids. The grids were stained with 2% uranyl acetate for 45 seconds, blotted out and dried overnight before imaging. The images were acquired on Tecnai^{TM} Spirit TEM (T12 Spirit, FEI, USA).

Fluorescence microscopy

*r*MrCP20 was labeled with FITC (Fluorescein isothiocyanate, Sigma-Aldrich) according to protocol prescribed by Sigma-Aldrich. Briefly, 3 mg/mL of FITC was dissolved in acetone and 200 μL was added dropwise to 8 mg/mL of *r*MrCP20 in 20 mM Tris and 150 mM NaCl buffer, incubated overnight. The reaction mixture was then subjected to PD-10 gel filtration column (GE healthcare life sciences) and eluted with 0.1 M $CaCl_2$. The FITC- *r*MrCP20 in 0.1 M $CaCl_2$ was then incubated with 0.1 M $NaHCO_3$ for four days and the resulting crystals were imaged. The images were obtained with inverted microscope (Zeiss Axio observer, Z1).

Results and Discussion

Vaterite mineralization by rMrCP20

The morphology of $CaCO_3$ crystals formed by *in vitro* mineralization was first analyzed using FESEM. In the absence of *r*MrCP20, FESEM observations showed a crystal morphology consistent with classic rhombohedral crystals of calcite for all observation times (Figure 1 a-d). In contrast, spherulites were observed in the presence of *r*MrCP20, suggesting the formation of vaterite polymorphs (Figure 1 e-h).

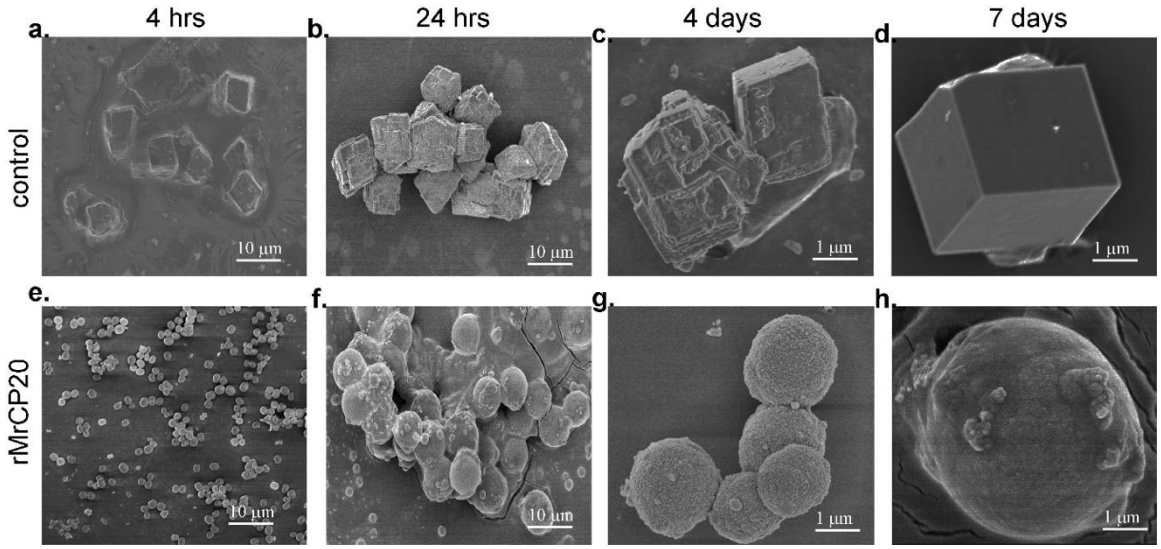

Figure 1. FESEM images of $CaCO_3$ crystals grown in the absence and presence of *r*MrCP20 at different time points. a-d. In the absence of *r*MrCP20, the rhombohedral crystal morphology is typical of calcite. **e-h**. In the presence of *r*MrCP20, the crystals have a spheroid shape reminiscent of vaterite.

To study whether supersaturation conditions of carbonate ions affected the crystal morphology, 4 mg/mL of *r*MrCP20 was incubated in $CaCl_2$-to-$NaHCO_3$ molar ratios of 1:0.5, 1:1; and 1:5 at a fixed $CaCl_2$ concentration of 0.1 M for 4 days. Under conditions of deficient carbonate concentration (1:0.5 $CaCl_2$-to-$NaHCO_3$ molar ratio), there were hollow spherical crystals (Figure S1a), which may be attributed to incomplete transformation of ACC to vaterite[41]. However at large relative carbonate concentration (1:5 molar ratio), elongated vaterite-like particles were obtained (Figure S1c). Hence all the further studies were conducted with equimolar (1:1) concentrations of $CaCl_2$ and $NaHCO_3$ where the spherulite morphology was observed (Figure S1b).

Next, the fate of *r*MrCP20 during vaterite mineralization was studied by labelling *r*MrCP20 with the FITC fluorescence tag at the N-terminus and incubating it with 0.1 M $NaHCO_3$ for four days, allowing to observe the location of *r*MrCP20 by fluorescence microscopy. As shown in Figure S2, the vaterite crystals observed by light microscopy overlapped with the fluorescence images, indicating that the *r*MrCP20 was embedded within the vaterite crystals. However, it is interesting to note that the concentration of MrCP20 was higher on the periphery of the vaterite crystals.

In order to verify the polymorphism of *r*MrCP20-mediated $CaCO_3$ crystals, we conducted ATR-FTIR and Raman spectroscopy measurements. As shown in Figure 2a, the control sample (free of *r*MrCP20) displayed vibrational peaks characteristic of

calcite, *i.e.* 715 cm^{-1} (ν4), 1396 cm^{-1} (ν3) and 875 cm^{-1} (ν2). On the other hand, after 4 h of incubation in the presence of *r*MrCP20, the spectra displayed a mix of calcite (a small shoulder at 715 cm^{-1} and ν3 peak at 1396 cm^{-1}) and vaterite (750 cm^{-1} and a shoulder at 1475 cm^{-1}) peaks. As the incubation period extended to 4 and 7 days, the intensity of calcite peaks strongly decreased (in particular the ν3 peak at 1396 cm^{-1}) and the spectra were dominated by vaterite peaks (Figure 2 a).

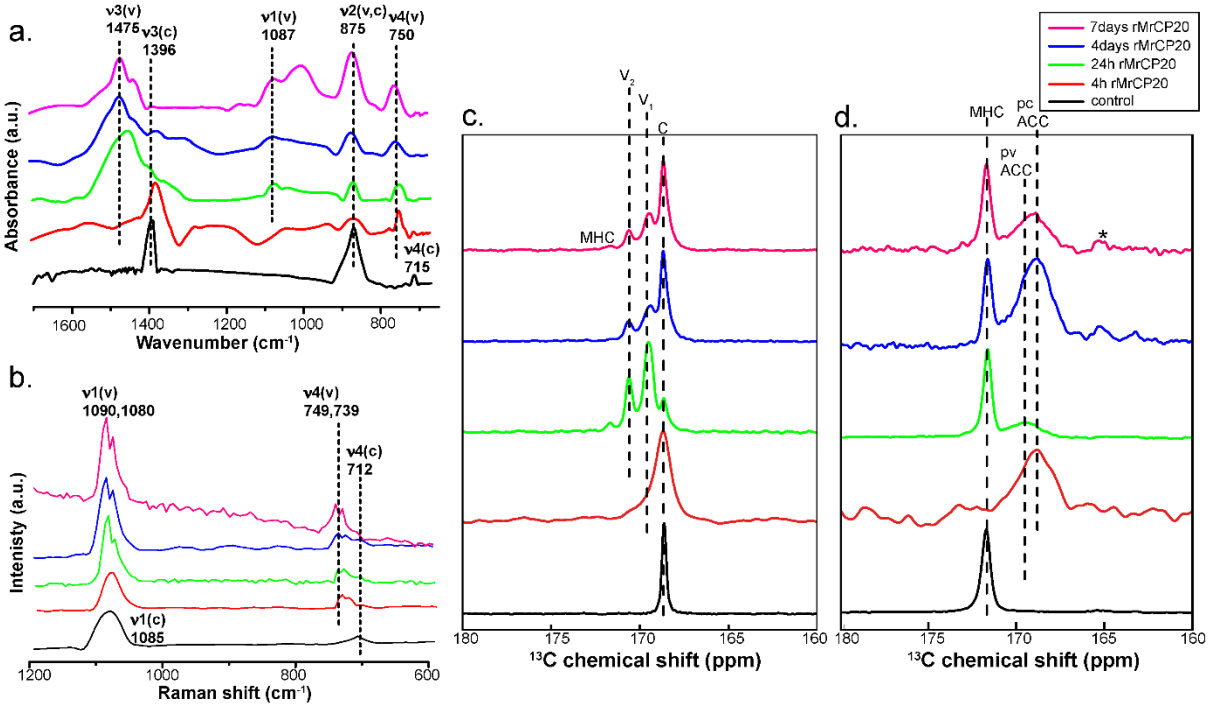

Figure 2. Spectroscopic analysis of $CaCO_3$ crystals. a. ATR-FTIR spectra of $CaCO_3$ crystals without (black) and with (colored) *r*MrCP20 incubated for various time periods. **b**. Raman spectra of $CaCO_3$ crystals of control sample (black) in comparison with (colored) *r*MrCP20 samples incubated for appropriate time periods. **c**. ^{13}C direct excitation MAS spectra of $CaCO_3$ crystals formed in the presence of *r*MrCP20 to identify calcium carbonate phases with control (black). C – calcite, V_1 and V_2 – vaterite and MHC – monohydrocalcite resonances. **d**. ^{1}H-^{13}C CP MAS spectra of $CaCO_3$ crystals formed by *r*MrCP20 (black stars exhibit traces of $NaH^{13}CO_3$ precursor of the mineralization reaction). pv-ACC – protovaterite amorphous calcium carbonate and pc-ACC – protocalcite amorphous calcium carbonate. ^{13}C resonances assignment was done according to Ref. [42]

The predominance of vaterite in the presence of *r*MrCP20 was corroborated using Raman spectroscopy measurements (Figure 2b). In the control sample, the only peaks that were detected were those characteristic of calcite at 1085 cm^{-1} (ν1) and 712 cm^{-1}(ν4) [43]. In the presence of *r*MrCP20 for 4 h of incubation time, the spectrum displayed a mixture of calcite and vaterite peaks. At longer exposure times, the vaterite peaks became more prominent, in particular the doublet peaks at 1080/1090 cm^{-1} and 739/749 cm^{-1} assigned to ν1 and ν4 vibration modes, respectively[43] (Figure 2b).

Further, we used ^{13}C solid state MAS (magic angle spinning) NMR spectroscopy to analyze calcium carbonate phases at the atomic scale and follow the precipitation sequence. First, ^{13}C DE MAS experiments were used to identify and quantify the various $CaCO_3$ phases according to the ^{13}C resonance positions and intensities. After 4 h of incubation, ^{13}C DE MAS NMR spectrum displayed a broad resonance at 168.6 ppm characteristic of well-crystallized calcite [49] and a weak shoulder at 169.5 ppm, the ^{13}C chemical shift of vaterite (Figure 2c, red peak). As the incubation continued, the characteristic doublet peaks (169.5 and 170.5 ppm) [49] of vaterite appeared clearly and became prominent with a relative intensity maximum after 24 h of incubation (Figure 2c, green) indicating 81% of vaterite. From 1 to 4 days of incubation, the proportion of well-crystallized calcite increased (from 10 to 60%) whereas a small amount (2-3%) of monohydrocalcite (MHC) was also observed. Then, the proportion of the different phases became stable from 4 to 7 days. On the other hand, the control samples exhibited a sharp resonance at 168.6 ppm indicative of well-crystallized calcite at all incubation times (Figure 2c, Figure S3a).

Then, ^{1}H-^{13}C CP MAS experiments were conducted to identify key transient phases (including ACC - polyamorphic phases,) as they display a strong ^{1}H environment. Critically, ^{1}H-^{13}C CP MAS experiments revealed the presence of phases in small proportion that could not be detected in ^{13}C DE MAS experiments. The samples incubated with *r*MrCP20 for 4 h displayed a broad ACC peak centered at 168.8 ppm (line width, LW = 2.1 ppm/160 Hz) corresponding to protocalcite ACC (pc-ACC), the precursor of calcite detected through ^{13}C DE MAS experiments (Figure 2d, red spectrum). In line with the previous observations, the 24 h sample displayed a broad protovaterite (pv-ACC) peak at 169.6 ppm[12] (LW = 2.1 ppm/160 Hz)[44] (Figure 2d, Figure S3c). As the incubation increased to 4 and 7 days, the broad ACC resonance was dominated by the pc-ACC contribution, in agreement with ^{13}C DE MAS spectra which evidence calcite as the dominant phase. We also note that from 4 to 7 days, the line width of the ACC peak decreased from 2.1 to 1.8 ppm (160 to 135 Hz), indicating structuration of the ACC phase probably linked to its ongoing crystallization (Figure S3c). In the absence of *r*MrCP20, the ^{1}H-^{13}C CP MAS NMR spectra revealed pc-ACC resonance (168.8 ppm) in agreement with ^{13}C DE MAS NMR data (Figure S3b).

Putting aside the 4 h experiments, in which the presence of calcite is likely related to a faster reaction kinetics between calcium and carbonate ions compared to the sequestration of these ions by *r*MrCP20, ^{13}C NMR experiments suggest the following reaction sequence. In the presence of *r*MrCP20, the formation of pv-ACC is favored (Figure 2d) and subsequently transforms into vaterite crystals (Figure 2c). As the incubation period progressed, we noticed an increase in calcite content. Here we speculate two possibilities: *(i)* as the *r*MrCP20 is depleted during prolonged

incubation, a second round of calcite precipitation occurs (Figure 2c, magenta spectrum); or *(ii)* vaterite starts to transform into the more stable $CaCO_3$ polymorph *i.e.* calcite[45].

Morphogenesis studies of vaterite mineralization by *r*MrCP20

The first intermediate stages of $CaCO_3$ mineralization were further studied to better understand the pathway mediated by biomolecular matrix *i.e r*MrCP20. To this end, we conducted solution NMR spectroscopy to analyze the phase transition observed during *r*MrCP20-induced mineralization. We used ^{13}C-labelled sodium bicarbonate ($NaH^{13}CO_3$) as source of carbonate ions, and followed the mineralization process by adding equal volume of *r*MrCP20 in the $CaCl_2$ solution and recording the spectra every 5 mins. As seen in Figure 3a, the initial carbonate peak at 161.95 ppm was severely distorted from the first 5 minutes and shifted to lower frequency with increasing incubation time. The distorted carbonate peak in the presence of a polymer has previously been assigned to a liquid condensed phase (LCP)[18]. Hence, the gradual appearance of the shoulder peak could be associated with clustering of Ca^{2+} and CO_3^{2-} ions enriched with *r*MrCP20 (Figure 3a, dotted line) separating from the bulk carbonate ions.

Furthermore, the overall displacement of chemical shifts to lower frequency can be explained by the pH drift during the formation of $CaCO_3$ as also observed by So *et al*[39]. In the presence of negatively charged polymers such as poly-aspartate, the initial reduction in pH can be related to the formation of PNCs, which consume carbonate ions as they bind to calcium ions[18], thus releasing protons from sodium bicarbonate and leading to a pH drift. Consistent with the mineralization reaction, the

intensity of the CO_2 peak (127.4 ppm) (Figure 3a, inset) increased over time. After 60 mins, only a minimal shift was observed, indicating that the transient liquid phase had solidified, thus becoming invisible in solution NMR experiments. In the absence of *r*MrCP20 (Figure 3b), the peak distortion started to arise only after 30 mins and continued to evolve until 90 mins indicating the slow evolution of LCP in the absence of the biomolecular matrix.

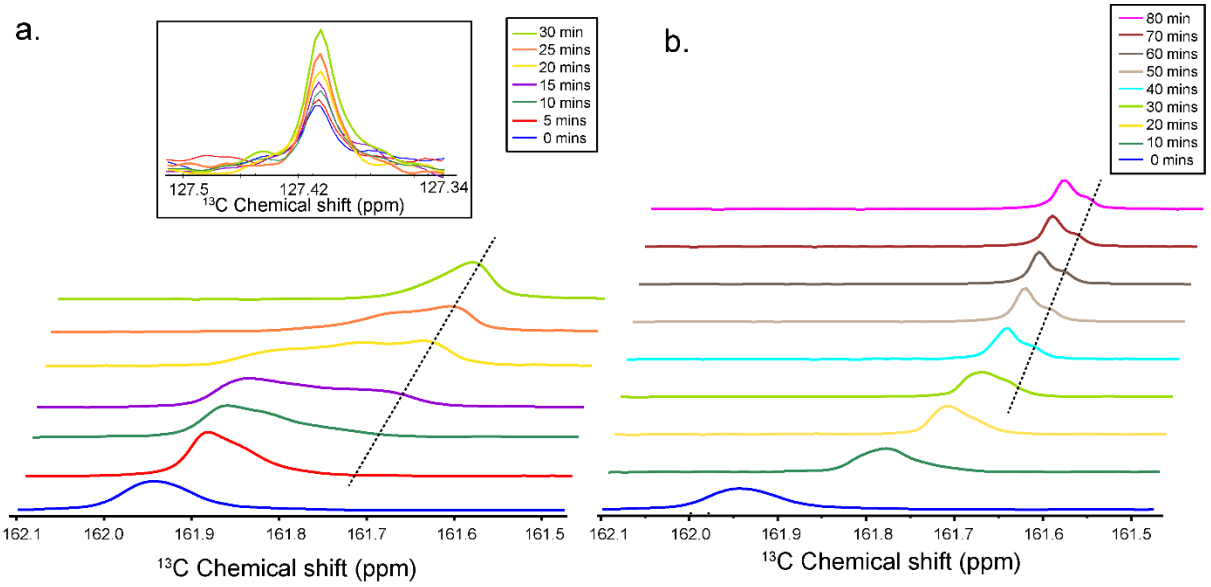

Figure 3. Phase transition of $CaCO_3$ particles monitored by solution NMR a. 1D ^{13}C NMR spectra of $NaH^{13}CO_3$ at $t = 0$ followed by addition of *r*MrCP20 in 0.1 M $CaCl_2$ (spectra taken every 5 mins). Inset: increase of CO_2 peak at 127.4 ppm with time. **b**. 1D ^{13}C NMR spectra of $NaH^{13}CO_3$ at $t = 0$ followed by addition of 0.1 M $CaCl_2$ (spectra taken every 10 mins).

The morphogenesis of early nuclei of $CaCO_3$ was imaged by AFM. Equimolar concentrations of $CaCl_2$ and $NaHCO_3$ were incubated in the presence or absence of *r*MrCP20 and aliquots were drawn at 30 mins, 1 h and 2 h for imaging. In the presence of *r*MrCP20, particles with size distribution of 50-500 nm were visible at all time points (Figure 4a). Based on solution NMR spectra (Figure 3a), we attribute these nanostructures to LCP droplets formed by the ion-sequestering activity of

*r*MrCP20 and subsequent formation of protovaterite-ACC (Figure 4a, *t* = 120 mins). In contrast, in the absence of *r*MrCP20, small nanoparticles that grew into protocalcite-ACC were clearly seen (Figure 4b).

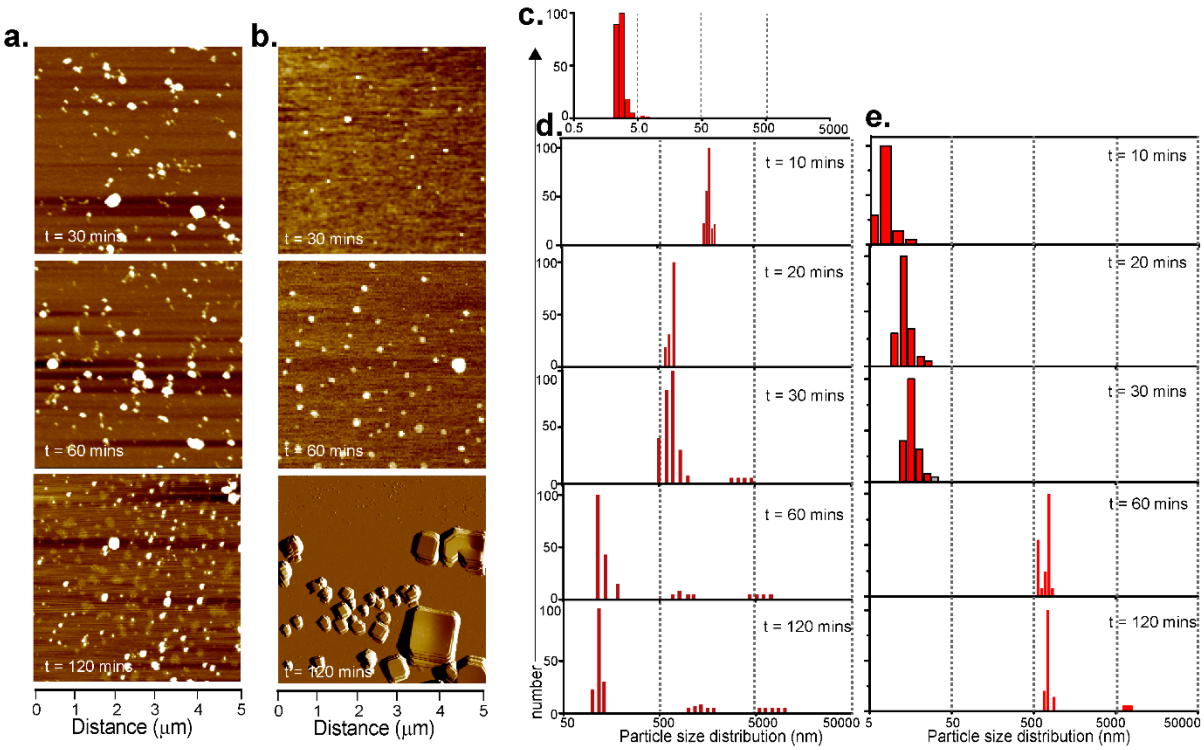

Figure 4. Morphogenesis studies of $CaCO_3$ crystals formed by *r*MrCP20. a-b. AFM images of initial $CaCO_3$ particles formed in the presence of *r*MrCP20 (left) and absence [13] at *t* = 30 mins, 60 mins and 120 mins. **c**. Particle size distribution measured by DLS (number distribution) of *r*MrCP20 in 0.1 M $CaCl_2$. **d-e** Particle size distribution measured by DLS (number distribution) of 0.1 M $CaCl_2$ incubated in 0.1 M $NaHCO_3$ solution at time periods mentioned in the presence (d) and absence (e) of *r*MrCP20. DLS spectra were measured every 5 mins until 60 mins and every 30 mins thereafter.

Measurement of the hydrodynamic diameter (D_H) by DLS further shed light on the formation of these precursors. The average size of *r*MrCP20 after addition of 0.1 M $CaCl_2$ was 2.8 nm[37] (Figure 4c). As soon as the 0.1 M $NaHCO_3$ solution was added, the particle size initially increased in the first 30 mins to reach around 650 nm (Figure 4d). The average size then started to decrease and stabilized at *ca*. 250 nm

until *t* = 6 h (Figure 4d, Figure S4a.). But a closer observation into the particle size distribution revealed the presence of larger particles (≥ 5000 nm) from *t* = 30 mins related to the nucleation of the solid phase. However, in the absence of *r*MrCP20, much smaller particles of around 15 nm attributed to PNCs (probably an aggregation of a limited number of PNCs according to the size) were observed in the initial 10 mins (Figure 4e). Then, a small increase in size to 30 nm was observed after 30 mins. Starting from 60 min, a transformation into larger objects of ~1 μm was observed due to solid nucleation, probability through clusters aggregation (Figure 4e, S4a). Overall, DLS studies suggest that in the presence of *r*MrCP20, solute PNCs of $CaCO_3$[11] quickly merge to form LCP droplets[18], which subsequently nucleate pv-ACC. During this nucleation process, the size of LCP droplets decreases as they are consumed by precipitation of pv-ACC (Figure S4 a, closed square).

The phase transition and its associated enthalpy changes were further evaluated by ITC experiments. The titration of the $CaCl_2$/*r*MrCP20 mixture in the injectant into $NaHCO_3$ resulted in a biphasic mode of binding, with an initial endothermic reaction (Figure S4b) until saturation of CO_3^{2-} ions was reached, followed by a second phase of exothermic binding (Figure S4b, inset) where there was an excess of $CaCl_2$/*r*MrCP20 mixture (the first ITC injection was neglected as it was used to establish equilibrium between the binding systems). A careful observation of the endothermic region revealed that as the Ca^{2+}-to-CO_3^{2-} molar ratio increased, the binding enthalpy increased until the 4th injection, explaining the possible formation of LCP droplets as noticed with DLS and AFM experiments. After which, the binding enthalpy decreased with increasing Ca^{2+} ion concentration, which may be attributed to dehydration-induced phase transition and subsequent spinodal decomposition to a

metastable state[11,18]. The second exothermic region may be attributed to self-assembly of *r*MrCP20 injected in excess after ACC formation in the endothermic region[49] (Figure S4b).

Overall, the morphogenesis studies suggest that the additive controlled nucleation and the PILP system works hand in hand, bringing about the polymorph selection. In the presence of *r*MrCP20, AFM and DLS studies revealed the formation of large LCP droplets at a faster rate that were detected as early as 10 mins. This observation is further supported with ^{13}C solution NMR spectroscopy studies, where the emergence of LCP was detected as early as 5 mins in the presence of *r*MrCP20. Smeets *et al.*[50] proposed that negatively-charged polystyrene sulfonate (PSS) sequesters calcium ions in such a way that immediate crystallization is delayed with ACC stabilization. Taken together, we propose that *r*MrCP20, with its high number of acidic residues, facilitate the clustering of inorganic ions, driving their assembly into liquid-like microdroplets that further stabilize into vaterite through transient pv-ACC.

Fibrillization of *r*MrCP20 proteins during $CaCO_3$ formation

Proteins rich in acidic amino acids such as Glu and Asp are well-known to attract positive Ca^{2+} ions and orchestrate the growth of $CaCO_3$ crystals[51]. For the particular case of *r*MrCP20, So *et al.*[39] have documented nanofibril formation in the glide symmetric crystal faces of calcite. Inspecting the morphogenesis of vaterite crystals by AFM, we noticed the presence of characteristic nanofibrillar structures in the background of the crystals appearing after 6 h of incubation time, which extended into fibrillar network after 24 h of incubation (Figures 5a-b). TEM imaging of negatively-stained *r*MrCP20 for the latter incubation time further confirmed the presence of these nanofibrillar features (Figure 5c). Deconvolution of the Amide I

band (1700-1600 cm^{-1}) of ATR-FTIR spectra of *r*MrCP20 in 0.1 M $CaCl_2$ in the absence of $NaHCO_3$ yielded the following semi-quantitative secondary structure composition: 32% helices, 38% beta structures, and 18% random coils (Figures. S5 a, c). After 24 h of incubation with 0.1 M $NaHCO_3$, we detected new peaks in the Amide I band, *i.e.* anti-parallel β-sheets (1685-1695 cm^{-1}) as well as a clear shoulder peak at 1615 cm^{-1} that can be assigned to cross-β amyloid[52-53]. Altogether, these data show that concomitant to regulating vaterite formation, *r*MrCP20 underwent a conformational transition towards nanofibrillar enriched in cross-β secondary structure.

In order identify the specific domains and residues of *r*MrCP20 that bind to inorganic ions and possibly exhibit conformational changes, a series of ^{1}H-^{15}N HSQC spectra were recorded with ^{15}N-labelled *r*MrCP20 in 0.1 M $CaCl_2$ incubated with and without $NaHCO_3$ (Figure 5d). The HSQC spectrum of *r*MrCP20/$CaCl_2$ was comparable to the native *r*MrCP20 spectrum[37], indicating that Ca^{2+} ions alone do not affect the structural features of *r*MrCP20. In contrast, one hour after addition of 0.1 M $NaHCO_3$, we noticed chemical shift changes in some of the key residues that occupy structural domains 2 (T^{82}-C^{112}) and 3 (C^{132}-H^{163}) (Figure 5e). We also identified Asp (D) as the main key amino acid recruiting inorganic ions since residues D^{68}, D^{79}, D^{158} (Figure 5f), D^{51}, D^{97} (Figure 5g) and D^{78} (Figure 5h) all showed evident chemical shift variations, thereby corroborating our recent MD results[40] where it was predicted that Ca^{2+} and CO_3^{2-} ions form clusters around the acidic-rich domains of MrCP20. Importantly, Cys residues C^{155} and C^{161} forming a disulfide bond that stabilizes the β-sheet of domain 3 in *r*MrCP20 exhibited a significant chemical shift (Figure 5g), consistent with reduction of the intra-molecular disulfide bond into free thiols. This

conformational change may be able to enhance the flexibility of β-strands 7 and 8 of *r*MrCP20 to facilitate inter-molecular registry required for cross-β fibrillization.

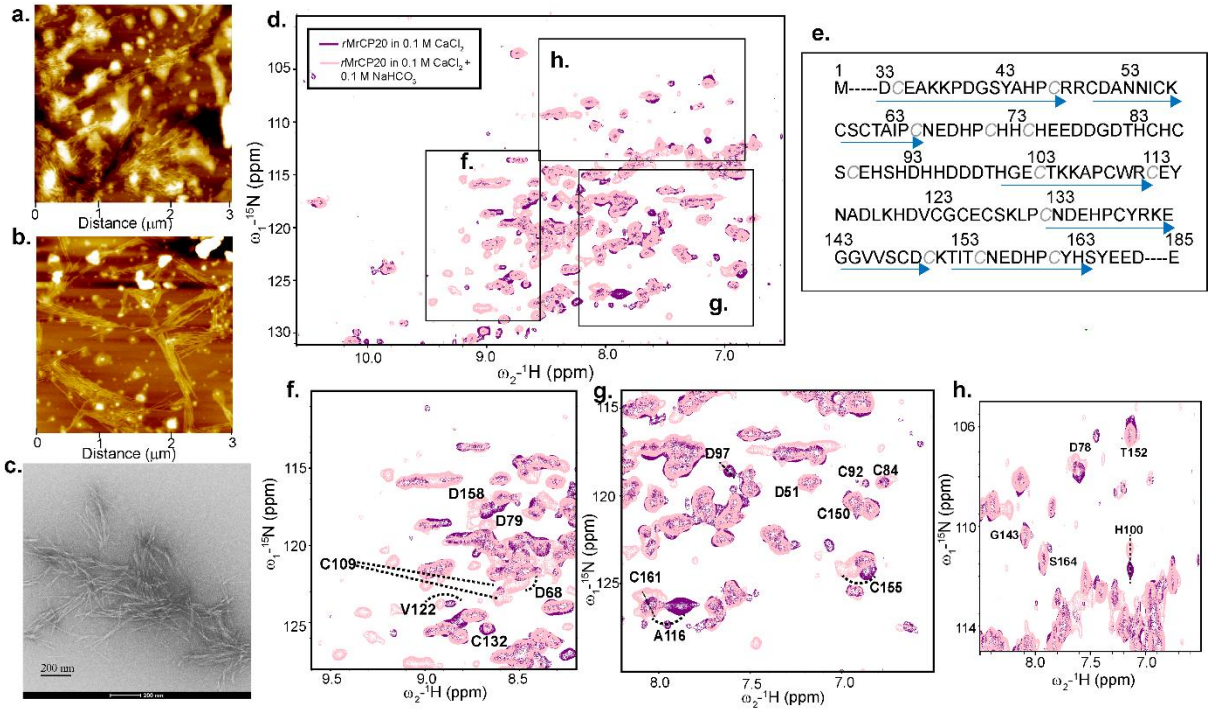

Figure 5. Self-assembly of *r*MrCP20 in the presence of calcium and carbonate ions. **a-b**. AFM images of *r*MrCP20 nanofibrils after 6 h (a) and 24 h (b). **c**. TEM image of uranyl acetate stained nanofibrils of *r*MrCP20. **d**. ^{1}H-^{15}N HSQC spectra of *r*MrCP20 in 0.1 M $CaCl_2$ in the absence (purple) and presence (pink) of 0.1 M $NaHCO_3$. **e**. Primary structure of *r*MrCP20 with the residues occupying β-strands underlined with blue arrows and disulfide bonded Cys highlighted in light grey. **f-h**. Enlarged regions of ^{1}H-^{15}N HSQC spectra of *r*MrCP20 in 0.1 M $CaCl_2$ in the absence (purple) and presence (pink) of 0.1 M $NaHCO_3$. Chemical shifts of amino acids showing characteristic shifts are marked based on the spectral assignment in Ref. [37]

Taken all data together, a model describing the synergistic fibrillization of *r*MrCP20 and vaterite stabilization can be proposed (Figure 6). In the first stage, *r*MrCP20 with its acidic-rich domains capture and stabilize clusters of Ca^{2+} and CO_3^{2-} as predicted by MD simulations[40]. In the presence of the *r*MrCP20 biomolecular matrix, the resulting LCP microdroplets trigger the nucleation of the solid phase dominated by pv-ACC. As the nucleation proceeds, pH drifts as result of proton

release, reducing disulfide bonds[54-55] and thereby enhancing the flexibility of β-strands of *r*MrCP20. This mechanism may facilitate intermolecular cross-β fibrillization, resulting in amyloid-like nanofibrils. Furthermore, our previous MD simulations predicted that water mediates carbonate binding to *r*MrCP20 through numerous H-bonds, resulting in water molecules at the protein/inorganic interface. Since amyloid fibrils have been documented to contain mobile water molecules[56-57], these may further stabilize the vaterite polymorph.

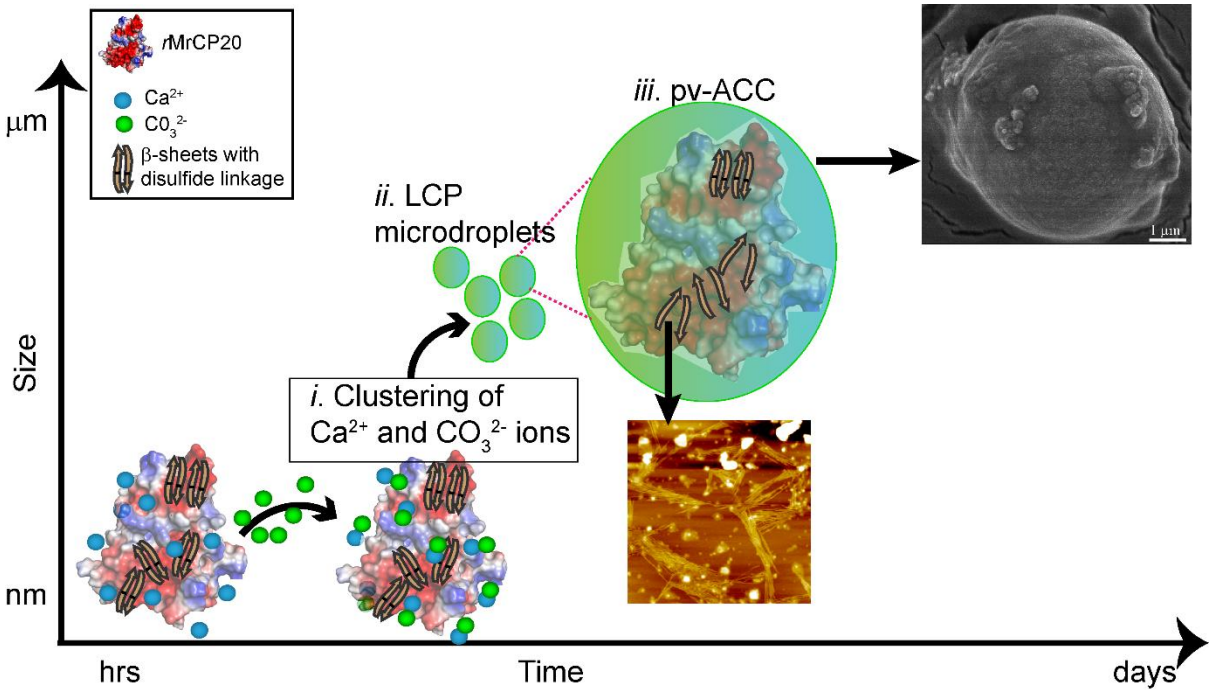

Figure 6. A model illustrating the steps involved in *r*MrCP20-mediated vaterite crystallization. *i.* Domains rich in acidic residues of *r*MrCP20 captures inorganic ions that aggregate into *ii*. *LCP* microdroplets. *iii.* Inside the droplets, two simultaneous processes take place, namely growth of cluster aggregates into pv-ACC and fibrillization of *r*MrCP20.

Conclusion

Our experimental results have revealed that *r*MrCP20 stabilizes vaterite through an articulated PILP pathway. We have shown that the biomolecular matrix of

*r*MrCP20 controls ACC nucleation through liquid condensed droplets, which in turn induce hierarchical assembly and fibrillization of *r*MrCP20. This mechanism is in agreement with previous studies reporting that long range amino acid interactions in β-sheets favor vaterite stabilization, with Ca^{2+} ions templating the side chains into a hexagonal lattice resembling that of vaterite[51]. Thus, we propose that fibrillization of *r*MrCP20 into amyloid-like nanofibrils plays a synergistic role of consolidating interfacial adhesion and stabilizing the vaterite polymorph during shell mineralization. Altogether, the mechanism of vaterite formation provides important insights in the regeneration/stabilization of exoskeleton of barnacles thriving in a multitude of environments.

Funding

H.M. and A.M acknowledge funding from the US Office of Naval Research – Global (ONR-G), grant no. N62909-17-1-2045 and the Singapore Ministry of Education (MOE) through an Academic Research Fund (AcRF) Tier 3 grant (# MOE 2019-T3-1-012). T.G and T.A acknowledge funding from CNRS through the NTU-CNRS “Excellence Science” joint research program (N° 294 382).

Author Contributions

H.M. performed all mineralization experiments and subsequent analyses by spectroscopic and microscopic methods. T.G. performed all ^{13}C solid state NMR experiments and analysis under the supervision of T.A. H.M and K.P. analysed solution state NMR data. H.M., T.G., T.A. and A.M. discussed and prepared the manuscript.

Acknowledgements

We thank Isaiah Chua for help with Raman spectroscopy, Zhi Wei for help with Fluorescence microscopy and Kimberly Low for help with TEM of *r*MrCP20 fibrils.

Conflict of Interest

The authors declare no competing interest with current work.

Supporting Information Description

The supporting information contains: SEM images of $CaCO_3$ at various super saturation conditions, Fluorescence images of FITC - *r*MrCP20, Solid state NMR spectra of control (free of *r*MrCP20), DLS and ITC profiles of early nucleation stage and deconvolution profile of amide I band of rMrCP20 with 0.1 M $CaCl_2$ and 0.1 M $NaHCO_3$.

References

1. Weiner, S.; Addadi, L., Crystallization Pathways in Biomineralization. *Annu. Rev. Mater. Res.* **2011,** *41* (1), 21-40.
2. Mann, S., *Biomineralization: Principles and Concepts in Bioinorganic Materials Chemistry*. Oxford University Press: New York, NY, USA, 2001.
3. Chave, K. E., Physics and Chemistry of Biomineralization. *Annual Review of Earth and Planetary Sciences* **1984,** *12* (1), 293-305.
4. Xu, A.-W.; Ma, Y.; Cölfen, H., Biomimetic mineralization. *Journal of Materials Chemistry* **2007,** *17* (5), 415-449.
5. Belcher, A. M.; Wu, X. H.; Christensen, R. J.; Hansma, P. K.; Morse, D. E., Control of Crystal Phase Switching and Orientation by Soluble Mollusc-Shell Proteins. *Nature* **1996,** *281*, 56-58.
6. Meyers, M.-A.; Chen, P. Y., *Biological Materials Science: Biological Materials, Bioinspired Materials, and Biomaterials*. Cambridge University Press: 2014.
7. Sabbides, T.; Giannimaras, E.; Koutsoukos, P. G., The precipitation of calcium carbonate in artificial seawater at sustained supersaturation. *Environmental Technology* **1992,** *13* (1), 73-80.
8. Henzler, K.; Fetisov, E. O.; Galib, M.; Baer, M. D.; Legg, B. A.; Borca, C.; Xto, J. M.; Pin, S.; Fulton, J. L.; Schenter, G. K.; Govind, N.; Siepmann, J. I.; Mundy, C. J.; Huthwelker, T.; De Yoreo, J. J., Supersaturated calcium carbonate solutions are classical. *Science Advances* **2018,** *4* (1), eaao6283.
9. De Yoreo, J. J., In-situ liquid phase TEM observations of nucleation and growth processes. *Progress in Crystal Growth and Characterization of Materials* **2016,** *62* (2), 69-88.
10. De Yoreo, J. J.; Gilbert, P. U. P. A.; Sommerdijk, N. A. J. M.; Penn, R. L.; Whitelam, S.; Joester, D.; Zhang, H.; Rimer, J. D.; Navrotsky, A.; Banfield, J. F.; Wallace, A. F.; Michel, F. M.; Meldrum, F. C.; Cölfen, H.; Dove, P. M., Crystallization by particle attachment in synthetic, biogenic, and geologic environments. *Science* **2015,** *349* (6247), aaa6760.
11. Gebauer, D.; Kellermeier, M.; Gale, J. D.; Bergström, L.; Cölfen, H., Pre-nucleation clusters as solute precursors in crystallisation. *Chemical Society Reviews* **2014,** *43* (7), 2348-2371.

12. Gebauer, D.; Gunawidjaja, P. N.; Ko, J. Y. P.; Bacsik, Z.; Aziz, B.; Liu, L.; Hu, Y.; Bergström, L.; Tai, C.-W.; Sham, T.-K.; Edén, M.; Hedin, N., Proto-Calcite and Proto-Vaterite in Amorphous Calcium Carbonates. *Angewandte Chemie International Edition* **2010,** *49* (47), 8889-8891.
13. Cartwright, J. H. E.; Checa, A. G.; Gale, J. D.; Gebauer, D.; Sainz-Díaz, C. I., Calcium Carbonate Polyamorphism and Its Role in Biomineralization: How Many Amorphous Calcium Carbonates Are There? *Angewandte Chemie International Edition* **2012,** *51* (48), 11960-11970.
14. Du, H.; Amstad, E., Water: How Does It Influence the CaCO3 Formation? *Angewandte Chemie International Edition* **2020,** *59* (5), 1798-1816.
15. Olszta, M. J.; Odom, D. J.; Douglas, E. P.; Gower, L. B., A New Paradigm for Biomineral Formation: Mineralization via an Amorphous Liquid-Phase Precursor. *Connective Tissue Research* **2003,** *44* (1), 326-334.
16. Gower, L. B.; Odom, D. J., Deposition of calcium carbonate films by a polymer-induced liquid-precursor (PILP) process. *Journal of Crystal Growth* **2000,** *210* (4), 719-734.
17. Gower, L., Biomimetic Model Systems for Investigating the Amorphous Precursor Pathway and its Role in Biomineralization. *Chemical Reviews* **2008,** *108*, 4551–4627.
18. Bewernitz, M. A.; Gebauer, D.; Long, J.; Cölfen, H.; Gower, L. B., A metastable liquid precursor phase of calcium carbonate and its interactions with polyaspartate. *Faraday Discussions* **2012,** *159* (0), 291-312.
19. Wolf, S. E.; Gower, L. B., Challenges and Perspectives of the Polymer-Induced Liquid-Precursor Process: The Pathway from Liquid-Condensed Mineral Precursors to Mesocrystalline Products. In *New Perspectives on Mineral Nucleation and Growth: From Solution Precursors to Solid Materials*, Van Driessche, A. E. S.; Kellermeier, M.; Benning, L. G.; Gebauer, D., Eds. Springer International Publishing: Cham, 2017; pp 43-75.
20. Zhang, G.; Yang, X.-X.; Leung, P. M.; He, L.-S.; Chan, T. Y.; Yan, G.-Y.; Zhang, Y.; Sun, J.; Xu, Y.; Qian, P.-Y., Secretory locations of SIPC in Amphibalanus amphitrite cyprids and a novel function of SIPC in biomineralization. *Scientific Reports* **2016,** *6* (1), 29376.
21. Dreanno, C.; Matsumura, K.; Dohmae, N.; Takio, K.; Hirota, H.; Kirby, R. R.; Clare, A. S., An α2-macroglobulin-like protein is the cue to gregarious settlement of the barnacle *Balanus amphitrite*. *Proceedings of the National Academy of Sciences* **2006,** *103* (39), 14396.
22. Raman, S.; Kumar, R., Construction and nanomechanical properties of the exoskeleton of the barnacle, Amphibalanus reticulatus. *Journal of Structural Biology* **2011,** *176* (3), 360-369.
23. Metzler, R. A.; O'Malley, J.; Herrick, J.; Christensen, B.; Orihuela, B.; Rittschof, D.; Dickinson, G. H., Amphibalanus amphitrite begins exoskeleton mineralization within 48 hours of metamorphosis. *Royal Society Open Science 7* (9), 200725.
24. Burden, D. K.; Spillmann, C. M.; Everett, R. K.; Barlow, D. E.; Orihuela, B.; Deschamps, J. R.; Fears, K. P.; Rittschof, D.; Wahl, K. J., Growth and development of the barnacle Amphibalanus amphitrite: time and spatially resolved structure and chemistry of the base plate. *Biofouling* **2014,** *30* (7), 799-812.
25. De Gregorio, B. T.; Stroud, R. M.; Burden, D. K.; Fears, K. P.; Everett, R. K.; Wahl, K. J., Shell Structure and Growth in the Base Plate of the Barnacle Amphibalanus amphitrite. *ACS Biomaterials Science & Engineering* **2015,** *1* (11), 1085-1095.
26. Jonsson, P. R., Wrange, A.L., Lind, U., Abramova, A., Ogemark, M., Blomberg, A, The Barnacle Balanus improvisus as a Marine Model - Culturing and Gene Expression. *Journal of Visualized Experiments* **2018,** *138*.
27. Wang, C.; Schultzhaus, J. N.; Taitt, C. R.; Leary, D. H.; Shriver-Lake, L. C.; Snellings, D.; Sturiale, S.; North, S. H.; Orihuela, B.; Rittschof, D.; Wahl, K. J.; Spillmann, C. M., Characterization of longitudinal canal tissue in the acorn barnacle Amphibalanus amphitrite. *PLOS ONE* **2018,** *13* (12), e0208352.
28. Kamino, K.; Shizuri, Y., Structure and Function of Barnacle Cement Proteins. In *New Developments in Marine Biotechnology*, Gal, Y. L.; Halvorson, H. O., Eds. Springer US: Boston, MA, 1998; pp 77-80.
29. Kamino, K.; Odo, S.; Maruyama, T., Cement Proteins of the Acorn Barnacle, Megabalanus rosa. *The Biological Bulletin* **1996,** *190* (3), 403–409.
30. Kamino, K., Mini review: Barnacle adhesives and adhesion. *Biofouling* **2013,** *29*+ (6), 735-749.
31. Kamino, K., Underwater Adhesive of Marine Organisms as the Vital Link Between Biological Science and Material Science. *Marine Biotechnology* **2008,** *10*, 111-121.

32. Kamino, K., Novel barnacle underwater adhesive protein is a charged aminoacid rich protein constituted by a cys-rich repetitive sequence. *Biochemical Journal* **2001,** *356*, 503-507.
33. Kamino, K., Molecular Design of Barnacle Cement in Comparison with Those of Mussel and Tubeworm. *The Journal of Adhesion* **2010,** *86*, 96-110.
34. Kamino, K.; Inoue, K.; Maruyama, T.; Takamatsu, N.; Harayama, S.; Shizuri, Y., Barnacle Cement Proteins. Importance of Disulfide Bonds in their Insolubility. *Journal of Biological Chemistry* **2000,** (275), 27360-27365.
35. Barlow, D. E.; Dickinson, G. H.; Orihuela, B.; Rittschof, D.; Wahl, K. J., In situ ATR–FTIR Characterization of Primary Cement Interfaces of the Barnacle Balanus amphitrite. *Biofouling* **2009,** *25* (4), 359–366.
36. Barlow, D. E.; Dickinson, G. H.; Orihuela, B.; Kulp, J. L., III; Rittschof, D.; Wahl, K. J., Characterization of the Adhesive Plaque of the Barnacle Balanus amphitrite: Amyloid-Like Nanofibrils Are a Major Component. *Langmuir* **2010,** *26* (9), 6549–6556.
37. Mohanram, H.; Kumar, A.; Verma, C. S.; Pervushin, K.; Miserez, A., Three-dimensional structure of Megabalanus rosa Cement Protein 20 revealed by multi-dimensional NMR and molecular dynamics simulations. *Philosophical Transactions of the Royal Society B: Biological Sciences* **2019,** *374* (1784), 20190198.
38. Mori, Y.; Urushida, Y.; Nakano, M.; Uchiyama, S.; Kamino, K., Calcite-Specific Coupling Protein in Barnacle Underwater Cement. *FEBS Journal* **2007,** *274* (24), 6436–644.
39. So, C. R.; Liu, J.; Fears, K. P.; Leary, D. H.; Golden, J. P.; Wahl, K. J., Self-Assembly of Protein Nanofibrils Orchestrates Calcite Step Movement through Selective Nonchiral Interactions. *ACS Nano* **2015,** *9* (6), 5782–5791.
40. Kumar, A.; Mohanram, H.; Li, J.; Le Ferrand, H.; Verma, C. S.; Miserez, A., Disorder–Order Interplay of a Barnacle Cement Protein Triggered by Interactions with Calcium and Carbonate Ions: A Molecular Dynamics Study. *Chemistry of Materials* **2020,** *32* (20), 8845-8859.
41. Kontrec, J.; Ukrainczyk, M.; Džakula, B. N.; Kralj, D., Precipitation and characterization of hollow calcite nanoparticles. *Crystal Research and Technology* **2013,** *48* (9), 622-626.
42. Behrens, G.; Kuhn, L. T.; Ubic, R.; Heuer, A. H., Raman Spectra of Vateritic Calcium Carbonate. *Spectroscopy Letters* **1995,** *28* (6), 983-995.
43. Donnelly, F. C.; Purcell-Milton, F.; Framont, V.; Cleary, O.; Dunne, P. W.; Gun'ko, Y. K., Synthesis of CaCO3 nano- and micro-particles by dry ice carbonation. *Chemical Communications* **2017,** *53* (49), 6657-6660.
44. Nebel, H.; Neumann, M.; Mayer, C.; Epple, M., On the Structure of Amorphous Calcium Carbonate—A Detailed Study by Solid-State NMR Spectroscopy. *Inorganic Chemistry* **2008,** *47* (17), 7874-7879.
45. Rodriguez-Blanco, J. D.; Shaw, S.; Benning, L. G., The kinetics and mechanisms of amorphous calcium carbonate (ACC) crystallization to calcite, viavaterite. *Nanoscale* **2011,** *3* (1), 265-271.
46. Oaki, Y.; Kajiyama, S.; Nishimura, T.; Imai, H.; Kato, T., Nanosegregated Amorphous Composites of Calcium Carbonate and an Organic Polymer. *Advanced Materials* **2008,** *20* (19), 3633-3637.
47. Xu, Y.; Tijssen, K. C. H.; Bomans, P. H. H.; Akiva, A.; Friedrich, H.; Kentgens, A. P. M.; Sommerdijk, N. A. J. M., Microscopic structure of the polymer-induced liquid precursor for calcium carbonate. *Nature Communications* **2018,** *9* (1), 2582.
48. Schenk, A. S.; Zope, H.; Kim, Y.-Y.; Kros, A.; Sommerdijk, N. A. J. M.; Meldrum, F. C., Polymer-induced liquid precursor (PILP) phases of calcium carbonate formed in the presence of synthetic acidic polypeptides—relevance to biomineralization. *Faraday Discussions* **2012,** *159* (0), 327-344.
49. Ikenoue, T.; Lee, Y.-H.; Kardos, J.; Yagi, H.; Ikegami, T.; Naiki, H.; Goto, Y., Heat of supersaturation-limited amyloid burst directly monitored by isothermal titration calorimetry. *Proceedings of the National Academy of Sciences* **2014,** *111* (18), 6654.
50. Smeets, P. J. M.; Finney, A. R.; Habraken, W. J. E. M.; Nudelman, F.; Friedrich, H.; Laven, J.; De Yoreo, J. J.; Rodger, P. M.; Sommerdijk, N. A. J. M., A classical view on nonclassical nucleation. *Proceedings of the National Academy of Sciences* **2017,** *114*, E7882-E7890.
51. Lu, H.; Lutz, H.; Roeters, S. J.; Hood, M. A.; Schäfer, A.; Muñoz-Espí, R.; Berger, R.; Bonn, M.; Weidner, T., Calcium-Induced Molecular Rearrangement of Peptide Folds Enables Biomineralization of Vaterite Calcium Carbonate. *J. Amer. Chem. Soc.* **2018,** *140* (8), 2793-2796.

52. Sarroukh, R.; Goormaghtigh E Fau - Ruysschaert, J.-M.; Ruysschaert Jm Fau - Raussens, V.; Raussens, V., ATR-FTIR: a "rejuvenated" tool to investigate amyloid proteins. (0006-3002 (Print)).
53. Huayan Yang, S. Y., Jilie Kong, Aichun Dong & Shaoning Yu Obtaining information about protein secondary structures in aqueous solution using Fourier transform IR spectroscopy. *Nature Protocols* **2015,** *10*, 382-396.
54. Tetsch, L.; Koller, C.; Dönhöfer, A.; Jung, K., Detection and function of an intramolecular disulfide bond in the pH-responsive CadC of Escherichia coli. *BMC Microbiol* **2011,** *11*, 74-74.
55. Hoffman, M. Z.; Hayon, E., One-electron reduction of the disulfide linkage in aqueous solution. Formation, protonation, and decay kinetics of the RSSR- radical. *J. Amer. Chem. Soc.* **1972,** *94* (23), 7950-7957.
56. Kim, Y. S.; Liu, L.; Axelsen, P. H.; Hochstrasser, R. M., 2D IR provides evidence for mobile water molecules in β-amyloid fibrils. *Proceedings of the National Academy of Sciences* **2009,** *106* (42), 17751.
57. Ke, P. C.; Zhou, R.; Serpell, L. C.; Riek, R.; Knowles, T. P. J.; Lashuel, H. A.; Gazit, E.; Hamley, I. W.; Davis, T. P.; Fändrich, M.; Otzen, D. E.; Chapman, M. R.; Dobson, C. M.; Eisenberg, D. S.; Mezzenga, R., Half a century of amyloids: past, present and future. *Chemical Society Reviews* **2020,** *49* (15), 5473-5509.